




Criticality in the fracture of silica glass: Insights from molecular mechanicsSomar Shekh Alshabab , Bernd Markert, and Franz Bamer ^{*}
Institute of General Mechanics, RWTH Aachen University, 52062 Aachen, Germany (Received 3 August 2023; accepted 2 February 2024; published 7 March 2024)

The universality of avalanches characterizing the inelastic response of disordered materials has the potential to bridge the gap from micro to macroscale. In this study, we explore the statistics and the scaling behavior of avalanches occurring during the fracture process in silica glass using molecular mechanics. We introduce a robust method for capturing and quantifying these avalanches, allowing us to perform rigorous statistical analyses, revealing universal power laws associated with critical phenomena. The influence of an initial crack is explored, observing deviations from mean-field predictions while maintaining the property of criticality. However, the avalanche exponents in the unnotched samples are predicted correctly by the mean-field depinning model. Furthermore, we investigate the strain-dependent probability density function, its cutoff function, and the interrelation between the critical exponents. Finally, we unveil distinct scaling behavior for small and large avalanches of the crack growth, shedding light on the underlying fracture mechanisms in silica glass.

DOI: [10.1103/PhysRevE.109.034110](https://doi.org/10.1103/PhysRevE.109.034110)**I. INTRODUCTION**

Predicting the fracture of disordered solids remains a long-standing research problem. In this context, statistical models have been extensively used to study the breakdown phenomena since they can address size effects and capture the fluctuations between different samples in real life [1].

Since fracture is a highly complex phenomenon that seems to originate from the finest details, the necessity for statistical treatment was recognized early on in the theory of Griffith that takes into consideration the random nature of the defects in the material [2]. Later, it was acknowledged that thermally activated fracture could be connected to first-order transition close to the spinodal point [3] so that efforts dealt with transition induced by disorder, where the quenched disorder plays the role of temperature [4].

When disordered solids are slowly driven by an external deformation field, their response is characterized by intermittent dynamics in the form of avalanches that increase in intensity before the breakdown of the material [5–7]. These avalanches originate from localized events [8] and follow power-law statistics that are also present in numerous natural processes beyond fracture and material science [9–12], suggesting a general mechanism of a more broad phenomenon. Predicting every microscopic event occurring during fracture turns out to be excruciatingly difficult and has been the focus of many studies using different approaches, including structural indicators [13], local shear modulus [14], harmonic and anharmonic approximation of the glass' energy [15,16], and machine learning [17]. However, statistical physics can explain the average behavior using simplified models that may capture the macroscopic response of a wide range of systems. These models are generally

treated in the mean-field framework [18] where many of the interaction details are washed away while a few relevant properties such as the underlying symmetries play the main role in deciding the leading terms of the expansion of the Landau-Ginzburg free energy [19] leading to different scaling relations.

Similar behavior has been observed for glasses as a major class of disordered solids with widespread applications in various fields due to their high strength and durability. On the nanoscale, (slowly driven) glasses under shear stress experience a steady-state phase which has been studied in the framework of self-organized criticality [20–23], while the yielding transition has mostly been studied with depinning models [24]. However, there is ongoing debate regarding the nature of this transition, with some researchers suggesting that it may belong to a different universality class [25,26]. Moreover, most molecular dynamics (MD) studies were performed on model glasses [27–31], or metallic glasses [32,33], while only a few focused on silica glass under shear [34] and even less on silica under tensile stress [35], where the yielding phase represented by the plastic steady state before failure is quite short-lived. Furthermore, the validity of the mean-field calculations remains under debate [36], with a wide range of computed critical exponents both numerically and experimentally [23,37,38]. Therefore, a realistic numerical model simulated with MD can be used as a powerful tool to get a better understanding of this complex behavior.

Silica glass which stands out as one of the most widely used materials, is brittle on the nanoscale making it susceptible to catastrophic failure under stress. Thus, its widespread use is severely limited by its cracking properties. Therefore, a better understanding of the failure mechanism can lead to the development of stronger and more fracture-resistant glasses and enables better and more efficient designs. The deformation behavior of silica is governed by its network topology [39], where the breakage of covalent bonds plays an

^{*}bamer@iam.rwth-aachen.de

important role in its inelastic response [40,41]. Furthermore, experimental studies have shown that cracks in silica glass grow in a sequential bond rupture without plastic deformation near the crack tip [42], while some other experimental [43] and molecular dynamic studies [44] claim that it breaks through the coalescence of nanoscale cavities and that plastic flow governs the cracking process [45]. Furthermore, it was shown that, the crack geometry exhibits the universal values of the crack roughness [44], providing further indication of the universality of the fracture process.

In this paper, we use molecular dynamics to study the fracture process of silica glass on the nanoscale under tensile stress, using the athermal quasistatic (AQS) deformation protocol for a wide range of system sizes including prenotched and unnotched systems. A new method is proposed in this paper for detecting and measuring the avalanches in the stress and energy of the system. Their statistics are analyzed and compared, showing that they follow power laws suggesting critical behavior. The critical exponents are determined by employing direct fitting and finite-size scaling (FSS) techniques. Additionally, we investigate the dependence of the probability density function (PDF) on the strain range, explore its cutoff function, and examine the relationship between the critical exponents. Finally, the crack growth process is captured, and the statistics of the corresponding avalanches are analyzed.

II. METHODS

A. Sample generation

We investigate the fracture of molecular systems using classical molecular mechanics. Four different system sizes of bulk silica were simulated, containing 6100, 12 150, 24 624, and 48 000 atoms. The largest system has the dimensions $88 \times 56 \times 140 \text{ \AA}$ and a density of 2.2 g/cm^3 . The other systems have approximately the same proportions and density. Each system was simulated by heating an ensemble to 8000 K. Subsequently, the temperature is kept constant using the NVT ensemble for 250 ps to ensure that, first, the samples reached a state of thermal equilibrium and, second, they have no memory of their initial configuration. The system is then rapidly quenched to a temperature of 0.01 K at the rate of 10 K/ps using the NVT ensemble. Finally, the samples are allowed to relax to a pressure-free state by iteratively altering the simulation box and minimizing the potential energy. We used a potential based on the Born-Mayer-Huggins potential, first proposed by Matsui [46], and reparameterized by Jakse *et al.* [47]. The potential between two atoms of type i and j is written as

$$U_{ij}(r_{ij}) = \frac{q_i q_j}{4\pi \epsilon_0 r_{ij}} + A_{ij} \exp\left(\frac{\sigma_{ij} - r_{ij}}{\rho_{ij}}\right) - \frac{C_{ij}}{r_{ij}^6}, \quad (1)$$

where r_{ij} is the interatomic distance, q_i refers to the effective charge, and A_{ij} and C_{ij} are parameters taken from Jakse *et al.* [47]. Equation (1) includes three terms: the Coulombic interaction term, short-range repulsive term (also known as the Born term), and the Van der Waals interaction term. The cutoff distance was set to 10.17 \AA .

B. Mechanical simulation

To investigate crack growth, an initial notch was introduced to the center of the samples by removing atoms from a cylindrical volume with an elliptical cross-section of $2.5 \times 5 \text{ \AA}$ in the xz plane which spans across the entire sample in the y direction. The size of the initial notch was chosen to be as small as possible while making sure that it constitutes a critical size for initiating failure. The samples are loaded uniaxially in the x direction at 0 K using the athermal quasistatic deformation protocol [48] with a strain step size of 10^{-4} . Notably, the step size was chosen small enough to make sure that all the avalanches occurring during deformation are recorded. The average time between the avalanches (weighting time) was measured for the biggest sample to be $\sim 2 \times 10^{-3}$.

Following the described methodology, 50 samples of each system size were generated and loaded until failure. A total number of 23 025 avalanche events were analyzed for the investigation of the energy drops, stress drops, and 11 253 events for the crack growth.

C. Void detection

To study the crack growth during mechanical testing, we used an external library [49,50] with which both the volume and the surface of the voids can be computed. In this paper, the voids were defined as the available space through which a hard sphere can move by assigning a spherical volume around every atom in the system. A diameter of 2 \AA was chosen for both the exclusion spheres around each atom and the moving hard-sphere taking into account the covalent bond distance between silicon and oxygen atoms.

D. Scaling

Three different quantities were chosen for the quantification of avalanche events: the intermittent drops in the virial stress during deformation $\Delta\sigma$, the drop in the potential energy $\Delta\Pi$, and the discrete jumps in the volume starting from the initial notch volume ΔV which identifies the crack growth.

Since the behavior in the response of the system changes with increasing strain, the conventional way of measuring avalanches, which is simply to evaluate the difference in the observed response magnitudes, such as stress or potential energy at two subsequent strain steps, leads to crucial inaccuracies for the present examples. On the one hand, it would lead to an overestimation in the avalanche size at the initial elastic regime, and, on the other hand, it would lead to an underestimation closer to the critical strain. In the case of steady flow as in a sheared glass, one could overcome this problem by correcting the drop according to the expected value in the case of a continued elastic behavior by using the elastic constant as follows $\Delta\sigma = \sigma_i - \sigma_{i+1} + E\Delta\varepsilon$ [51]. However, this is not straightforward in our case since the elastic constant changes significantly with increasing strain. Therefore, we propose an alternative method for measuring the avalanches wherein events are detected in terms of fluctuations in the studied quantity rather than by simply identifying the drops. To this end, the avalanches are identified as discontinuities in the change of the energy ($\Pi_i - \Pi_{i+1}$) or stress ($\sigma_i - \sigma_{i+1}$). Then a running average is constructed at the time steps

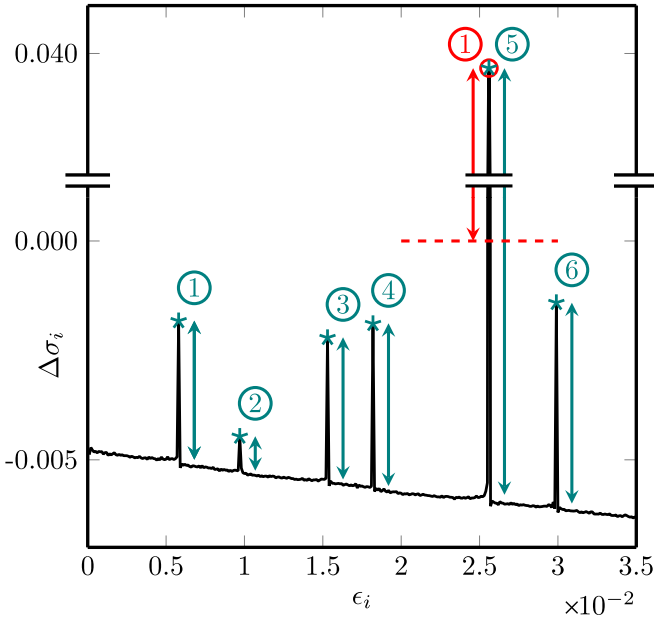


FIG. 1. Illustrative plot of the avalanche measurements. The black line represents the stress difference between two consecutive steps $\Delta\sigma_i = \sigma_{i+1} - \sigma_i$ as a function of the strain ε_i . The green color shows the detected avalanches if one considers a wider range of fluctuations, and the red color shows the detected avalanches if one defines avalanches as $\Delta\sigma_i > 0$. The arrows represent the avalanche magnitude of each method. The inclination in the black line shows how the elastic response of the material changes with increasing strain.

without events, and interpolated at the time of the events, which would correspond to a running average curve of the elastic constant E . Finally, the size of the avalanches is computed as the difference between the peaks and the running average curve. An illustration of the approach is shown in Fig. 1.

Taking into account the relevant literature published in fracture mechanics, we expect the avalanche statistics to follow a power law with a system size-dependent cutoff, cf. Refs. [4,25]. Based on this assumption, we initially computed the critical exponent from the simulations by direct fitting. However, it is known that fitting with the moments of the PDFs by assuming finite-size scaling yields better estimates, particularly when the statistical sample size is inadequate for determining the cutoff tail with precision [52]. Therefore, we carried out finite-size scaling analysis by investigating the moments of the distribution function from which we estimated the critical exponents. The validity of this assumption can be assessed by evaluating the quality of the resulting data collapse.

We assume that the PDF integrated over a certain strain domain scales as follows:

$$P(m) \sim N^{-\beta} f\left(\frac{m}{N^{\beta/\tau}}\right), \quad (2)$$

where N is the system size. Then, one expects the first moment of the PDF to scale as follows:

$$\langle m^a \rangle \sim N^{\frac{\beta}{\tau}(a+1-\tau)} \sim N^{\alpha(a)}. \quad (3)$$

This equation is only valid for values of $a + 1 - \tau > 0$, and it reads

$$\alpha(a) = \frac{\beta}{\tau}(a - \tau + 1), \quad \frac{\partial\alpha(a)}{\partial a} = \frac{\beta}{\tau}. \quad (4)$$

Therefore, the exponents τ and β can be computed from the log-log plot of $N - \langle m^a \rangle$, for different values of α , by following the method proposed by Chessa *et al.* [52].

To study the cutoff tail for the PDF, we rely on the scaling relations derived from the fiber bundle model (FBM) with the global load-sharing rule, which corresponds to the mean-field calculation for the fracture transition due to the infinite interaction length between the single fibers. Accordingly, we expect the PDF of the avalanche size to scale as follows:

$$P(m, \varepsilon) \sim m^{-\tau} e^{-Am(\varepsilon_c - \varepsilon)^\kappa}. \quad (5)$$

Here, m is the avalanche size, the strain ε plays the role of the external force field f , and ε_c is the critical strain. This relation is expected to be valid for small bin sizes; however, in our case, a much larger statistical sample size is needed, which poses a challenge. Therefore, we adopt a strategy of integrating the PDF over different strain regimes. By integrating from $\varepsilon = 0$ to $\varepsilon = \varepsilon_c$, it would take the following form:

$$P(m) \sim \frac{1}{\kappa} m^{-\tau'} \gamma(1/\kappa, Am\varepsilon_c^\kappa), \quad (6)$$

where $\tau' = \tau + 1/\kappa$ and γ is the lower incomplete gamma function. In the case of arbitrary bin sizes $\varepsilon_1 - \varepsilon_2$ it is written as

$$P(m) \sim \frac{1}{\kappa} m^{-\tau'} \{ \gamma[1/\kappa, Am(\varepsilon_c - \varepsilon_2)^\kappa] - \gamma[1/\kappa, Am(\varepsilon_c - \varepsilon_1)^\kappa] \}. \quad (7)$$

Finally, for any strain regime from 0 to ε , it is written as

$$P(m, \varepsilon) \sim m^{-\tau'} \{ \gamma[1/\kappa, Am(\varepsilon_c - \varepsilon)^\kappa] - \gamma[1/\kappa, Am(\varepsilon_c)^\kappa] \}. \quad (8)$$

Additionally, one may analyze the moments of the PDFs for different strain regimes, starting from Eq. (5). The average avalanche size would diverge as the system approaches the critical strain, according to the following scaling relation:

$$\langle m^a \rangle \sim (\varepsilon_c - \varepsilon)^{\kappa(\tau - a - 1)} \gamma[a + 1, Am_c(\varepsilon_c - \varepsilon)^\kappa], \quad (9)$$

where m_c is the critical avalanche size. We assume that it is related to the linear dimension $m_c \sim L^{d_f}$ or $m_c \sim N^{d_f/3}$ where d_f is the fractal dimension, or that $m_c \sim m_{\max}$. For the FBM, one expects the critical exponents to be $\tau = 1.5$ and $\kappa = 1.0$ [53].

We assume that preexisting defects in the material interact through long-range elastic fields [54]. This could lead to mean-field behavior even in dimensions lower than the lower critical dimension [55]. One may study the extent of the elastic fields by analyzing the load transfer in the system which is expected to decay exponentially as $1/r^\gamma$, where r is the interaction radius. In the fiber bundle model, the interaction range is infinite, and, therefore, the calculations correspond to the mean-field limit [56], while in the ones incorporating the local load sharing rule, γ defines the system response to the fiber breaking events, where $\gamma = 2$ forms the cross-over

between local and global behavior. The complete derivations of Eqs. (6) to (9) are presented in the Appendix.

III. RESULTS AND DISCUSSION

At low strains, the material exhibits nearly linear behavior, and only a relatively small number of plastic events was detected. These events increase in size and frequency with increasing strain until failure. All the simulations reveal brittle behavior. However, the ductility increases with decreasing system size due to size effects. Furthermore, a short steady state before failure was observed as expected from rather brittle materials. Since the presence of a long-lived absorbing phase represented by the steady state is an important criterion for self-organized criticality [57,58] one may argue that classifying the fracture of silica in the framework of self-organized criticality may not be feasible.

The nonaffine displacement fields for two avalanche events are plotted in Fig. 2. A small event is plotted in Figs. 2(a) and 2(b) where it can be seen that the event consists of two subevents interacting with each other through elastic fields. However, neither of them is at the edge of the initial notch. This observation highlights the role of the disorder of the system whereby not all events result in the propagation of the crack. Furthermore, the events shown take dipolar shapes with two distinct inclinations relative to the loading axis. The dipolar shape was predominant in our simulations, in contrast to events in shear loading regimes, which are characterized by quadrupolar shapes [59]. This difference in shape is known to impact the waiting time between avalanches [60]. In Figs. 2(c) and 2(d) a catastrophic event is plotted whose magnitude extends over the entire system and leads to failure of the system. It is worth noting that the power laws derived from the mean field of depinning models are expected to fail to capture the statistics of the large system-spanning events [61]. Moreover, the catastrophic events in the FBM are known to follow a Gaussian distribution [56].

The average strain interval between the avalanches decreases exponentially with the increasing system size as $\Delta\varepsilon \sim N^{-\chi}$ with $\chi \approx 0.4234$. Similarly, the critical strain is defined as the strain at which the average avalanche size diverges scales as $\varepsilon_c \sim N^{-B}$ with $B \approx 0.1025$. These results are plotted in Fig. 3.

By assuming that the average maximum avalanche from each system corresponds to the critical avalanche size, one can compute the fractal dimension from its dependence on the system size. The results are plotted in Fig. 3(a). One can see from the slope of the fitted line that $d_f/3 \approx 1.24$ and therefore $d_f \approx 3.72$. This is much larger than the typical values reported from statistical fracture models, which usually fall in the range between 1.0 and 1.25 [56].

It is worth pointing out that our systems are not ideally brittle since the fracture process involves substantial plastic deformations. Rountree *et al.* [62] made an intriguing observation on sheared glasses, showing that the glass undergoes permanent anisotropic changes in the Si-O-Si triplets. Following this line of thought, we measured the anisotropic change during the deformation, which is reflected in changes of the fabric tensor $\mathbf{F} = \langle \mathbf{n} \otimes \mathbf{n} \rangle$, where \mathbf{n} is the normal vector between Si atoms in neighboring tetrahedra. In this sense,

the largest eigenvalue corresponds to the principal stretching direction of the triplets. Therefore, we plot the x component of the eigenvector $v_{1,x}$ of the largest eigenvalue versus strain in Fig. 4. We find that $v_{1,x}$ increases rapidly after the initial phases of deformation. Then, the relation enters a slowly increasing linear phase until reaching its maximum value shortly before the crack initiates. During the linear phase, the principle stretching direction is almost completely parallel to the deformation direction. Furthermore, we measure the anisotropy induced by the remote field by computing the parameter defined as $\alpha = \frac{3}{2} \sqrt{\sum_{i=1}^3 (\lambda_i - \frac{1}{3})^2}$, where λ_i are the eigenvalues of the fabric tensor. As shown in Fig. 4, the anisotropy increases significantly for all the sample sizes but decreases to lower values after the full propagation of the crack. Interestingly, some degree of anisotropy remains even though the samples return to a stress-free state after fracture rather than to a strain-free state as in the original study by Rountree *et al.* [62]. This shows that irreversible processes other than the crack propagation take place even though the plastic flow phase is barely detectable in the stress-strain curves. For comparison, we also computed the anisotropy parameter based on the fabric tensor of Si-O couples. We found no significant irreversible changes after failure, indicating that the tetrahedra in the glass remain predominantly unchanged.

Furthermore, we study the fracture energy of the system defined as the energy dissipated per unit crack area following Griffith's classical assumptions [2]. First, we investigate the stress concentration around the crack tip shortly before the first propagation events start by computing the virial stress per atom. The stress decays away from the crack tip as $\sigma_{xx} \sim r^{-\gamma}$, with $\gamma = 0.52$ at $\varepsilon = 0.12$. We compute values for γ ranging from 0.48 to 0.55 for about 400 steps before the crack propagates. This hints at a universal stress field around the crack tip, possibly aligning with the prediction of Irwin's formula [63], where the stress decays as the inverse square root of the distance from the crack tip. The results are plotted in Fig. 5. It is important to note that the values of γ in the elastic deformation regime exceed 0.60, meaning that the stress decays slower around the crack tip. We attribute that to the inherent structural disorder, which competes with the initial notch for the stress concentration. However, at higher stresses, the localizing effect of the initial notch becomes dominant. To compute the fracture energy we rely on an energetic approach [64], where the critical energy release rate is evaluated as

$$G_c = \frac{L_x L_y L_z}{(A_\infty - A_0)} \int_0^{\varepsilon_x^{(\max)}} \sigma_x d\varepsilon_x. \quad (10)$$

Starting with the largest and progressing to the smallest system, we obtained fracture energies of $J = 3.04, 2.76, 2.84,$ and 2.84 Joule/m². Notably, these values are smaller than the macroscopically experimentally measured values of silica glass. However, our simulations were performed in the athermal limit, so these values cannot be directly compared. Furthermore, we quantify the amount of the dissipated energy during deformation. It captures about 77.09%, 74.89%, 76.44%, and 79.86% of the total mechanical work of the system, for the systems with 48 000, 24 624, 12 150, and 6100 atoms, respectively. The remaining portion remains stored in the system.

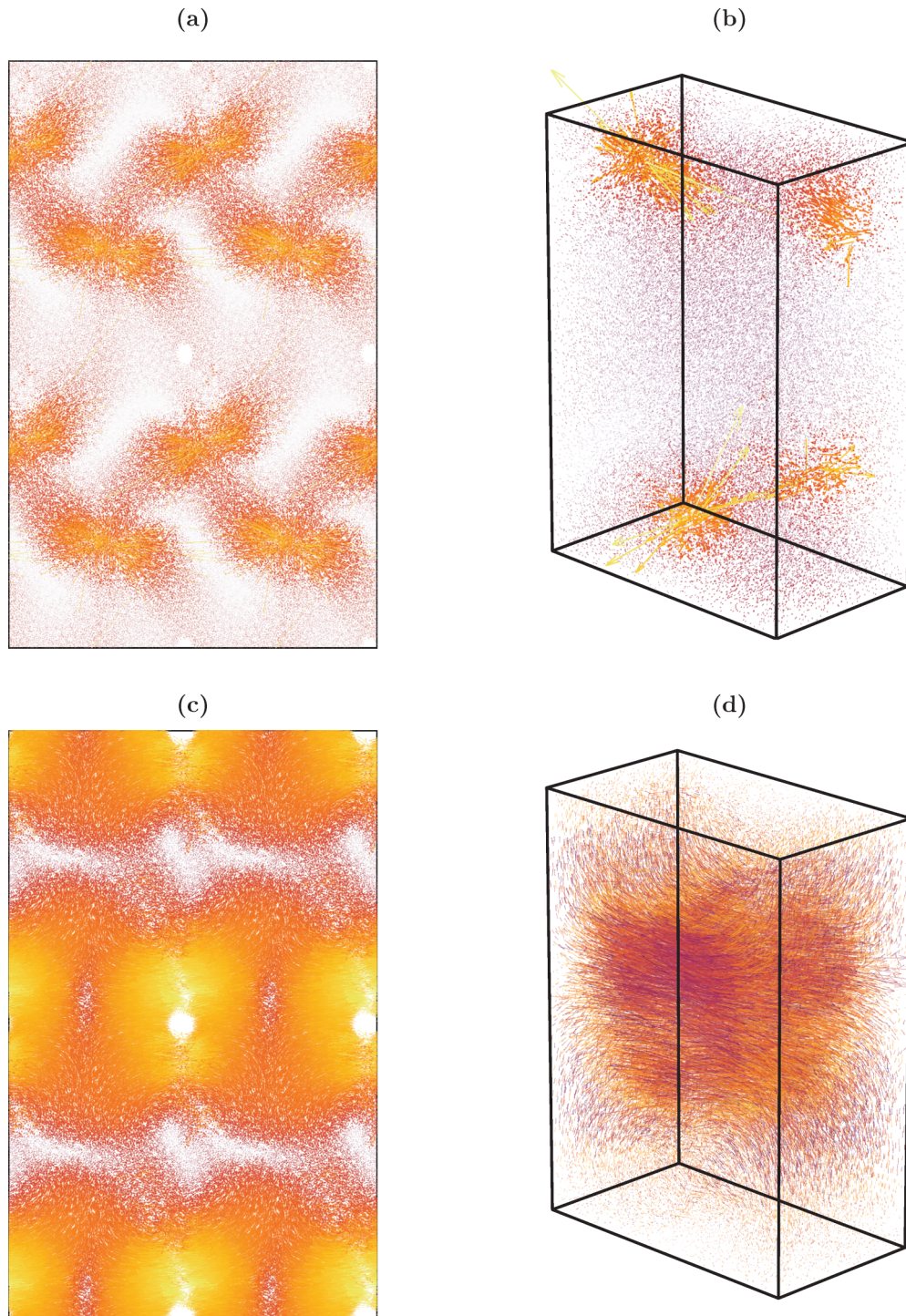


FIG. 2. Nonaffine displacement field for two events in the system with 48 000 atoms. (a) A small event in the elastic strain regime projected on the xz plane. (b) The same event in three dimensions. (c) The largest event during loading projected on the xz plane, leading to the propagation of the initial crack. (d) The same event in three dimensions. The arrows and colors are normalized and scaled logarithmically. Hence, the events are more localized than they appear in the plots. Additionally, the plots are replicated in both the x and z directions in (a) and (c) to demonstrate the periodic boundary conditions.

We expect these percentages to rise in the presence of the temperature since an essential part of the energy is dissipated through temperature, resulting in a higher cost for the creation of new surfaces with the crack propagation.

Avalanches

Our analyses confirm the occurrence of scale-invariant avalanches. In Fig. 6, the probability distribution function $P(\Delta\Pi)$, taking into account the strain domain from zero until the critical strain, is plotted. The avalanches follow a power

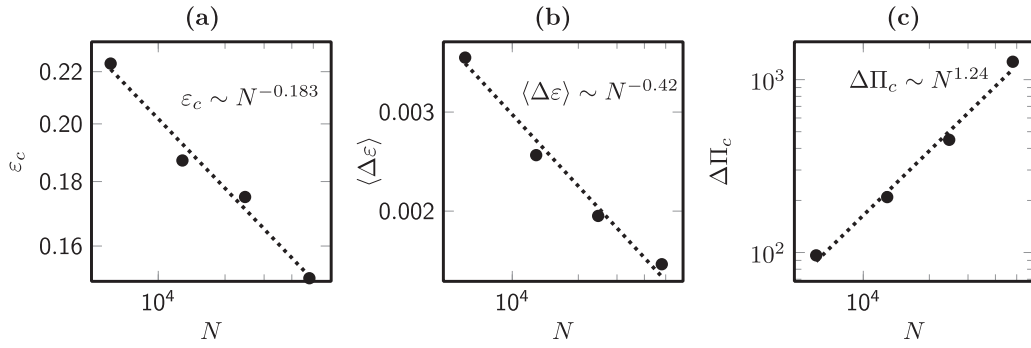


FIG. 3. Dependence of (a) the critical strain, (b) the average waiting time between the energy avalanches, and the critical avalanche size on the system size.

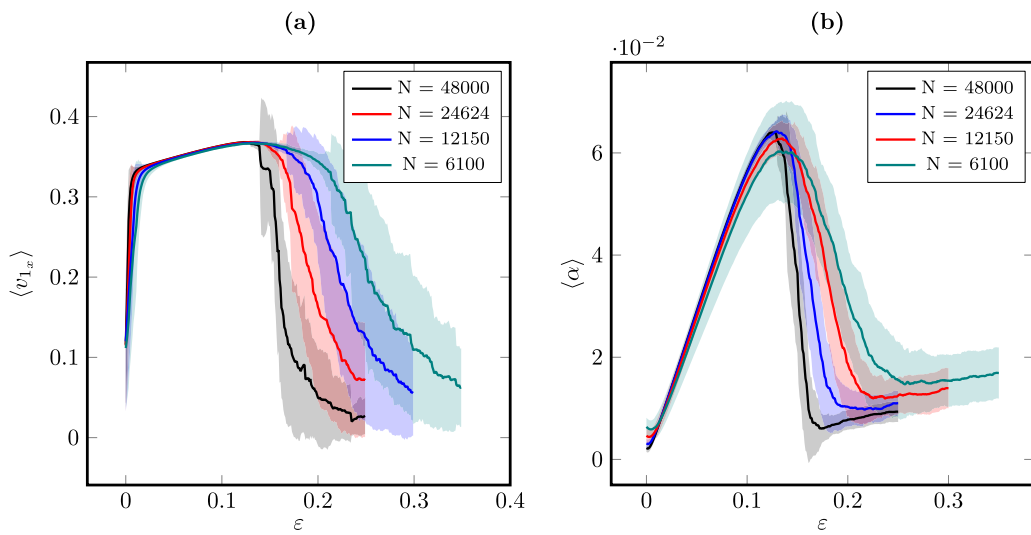


FIG. 4. Change in the anisotropy during the tensile simulations. (a) The horizontal component of the first eigenvector of the fabric tensor. (b) The anisotropy parameter. The solid lines represent the average over the different samples, while the shaded areas represent the standard deviation.

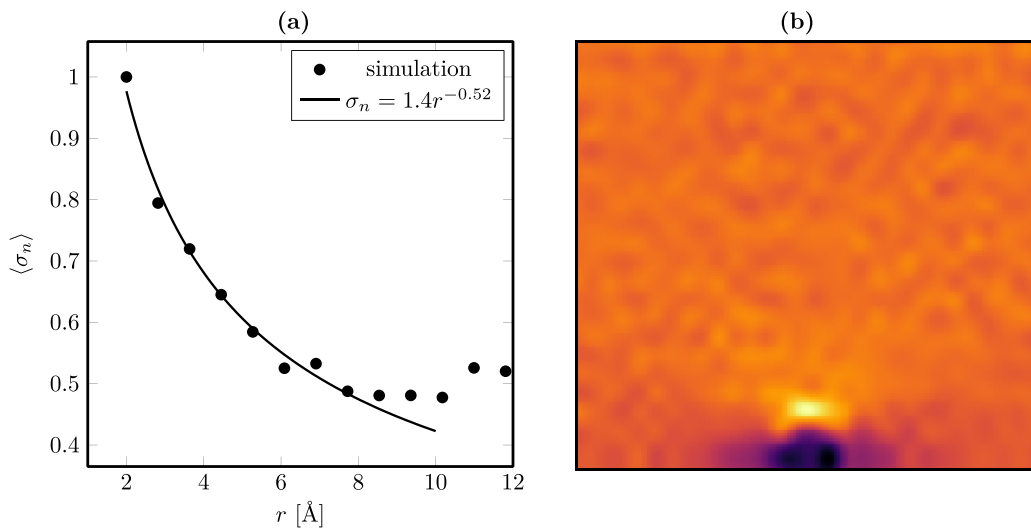


FIG. 5. Stress field around the crack tip for the largest system. (a) Decay of the of the average normalized stress $\langle \sigma_n \rangle$ away from the crack tip at strain $\epsilon = 0.12$ shortly before crack propagation starts. (b) Interpolated normalized virial stress field averaged over all the samples.

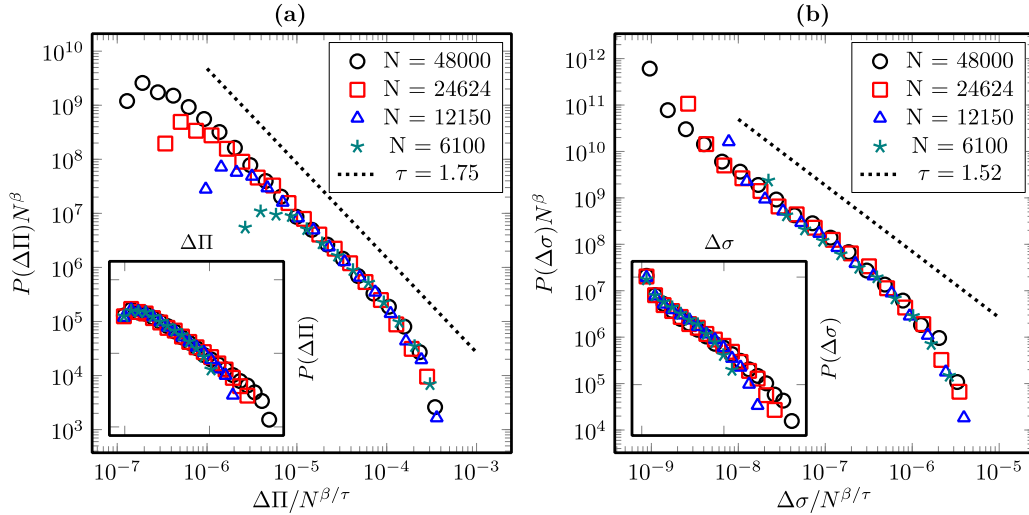


FIG. 6. Scaled probability distribution function for the (a) energy and (b) stress avalanches. Inset: The unscaled PDF. The data collapse indicates a good fit for the computed exponents from FSS. The avalanches are integrated over the strain regime until the critical strain. The black line represents a power law $m^{-\tau'}$ where the critical exponent τ' is computed from the first moment analysis of the distribution function.

law with cutoffs at both ends of the PDF. The upper cutoff is exponential and scales with the system size. We find through the direct fitting of the sample containing 48 000 atoms that the critical exponent takes a value $\tau'_{\Delta\Pi} \approx 1.75$. However, to confirm this value, we carry finite-size analyses by assuming a scaling function in the form $P(\Delta\Pi) \sim N^{-\beta} f(\Delta\Pi/N^{-\beta/\tau'})$. By analyzing the first moment of the PDF, we evaluated $\beta_{\Delta\Pi}/\tau'_{\Delta\Pi} = 1.47$ from the derivative $\partial\alpha(a)/\partial a$, which was computed from the slope of the logarithmic plot of $N - \langle m^\alpha \rangle$. Subsequently, $\tau'_{\Delta\Pi} = 1.75$ was evaluated from the relation $\alpha(a) = \beta/\tau'(a - \tau' + 1)$, so that $\beta_{\Delta\Pi} = 2.57$. Finally, to validate our calculations, we collapse the data with the hypothesized function and the computed exponents in Fig. 6. As shown in this figure, the collapse is satisfactory since the data points of the PDFs of the different system sizes fall into one curve.

Similarly, the probability distribution function of the stress drops $P(\Delta\sigma)$ is plotted in Fig. 6(b). A power law is observed with cutoffs at both ends, with the upper cutoff being dependent on the system size. We compute $\tau'_{\Delta\sigma} \approx 1.50$ through direct fitting of the biggest system. Subsequently, we computed through FSS $\tau'_{\Delta\sigma} = 1.52$ and $\beta_{\Delta\sigma} = 2.52$, following the same procedure as for the energy avalanches. For comparison, if the avalanche measurement is considered as a simple difference in stress before and after the event, the statistics show a strong bias in the power, contradicting the criticality assumption of the avalanches, as shown in Fig. 7. The fractal dimension can be estimated also from FSS since we know that the value β/κ should correspond asymptotically to d_f/d , where $d = 3$ is the spatial dimension of the system. Accordingly, we find that the fractal dimension computed from energy avalanches $d_f \approx 4.4$ confirms that the critical dimension in our systems is much larger than the expected range. Equally, we demonstrate that crack growth occurs in avalanches following a power law. However, the avalanches appear to deviate from a simple power law and exhibit a multifractal distribution, in particular, a double power law. This can be seen in Fig. 8, where the probability density function $P(\Delta V)$ is presented. Direct

fitting of critical exponents for the biggest system shows that $\tau_{\Delta V_1} = 0.9$ for the first and $\tau_{\Delta V_2} = 2.0$ for the second regime.

So far, our results were obtained from the PDFs of the events recorded over a strain period from 0 to ε_c . However, the critical exponent τ from Eq. (5) can be obtained by plotting the recorded avalanches at any strain value and over a very small strain range. However, the effect of the exponential cutoff would get stronger as one gets further away from the critical strain [56]. Therefore, τ could be evaluated by recording the avalanches as close as possible to the critical strain with a range that is as small as possible while still having

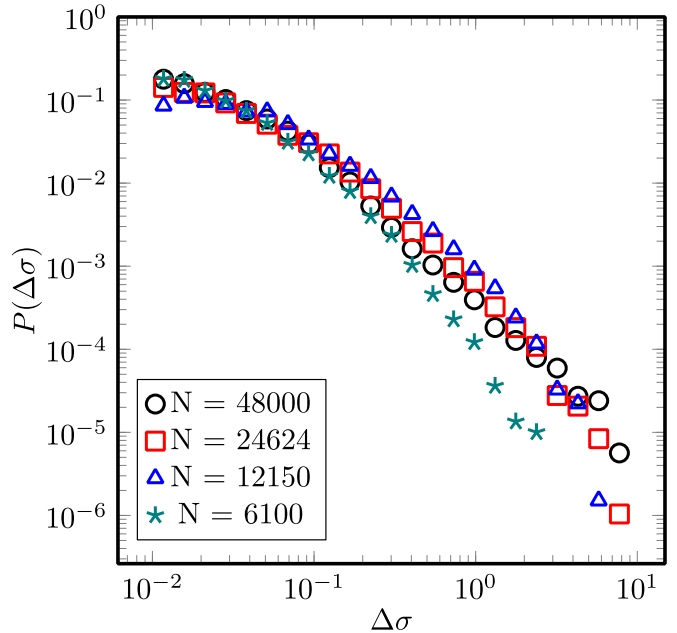


FIG. 7. Probability distribution function for the stress avalanches when the measurement is taken as the simple stress drop without stiffness-based corrections. This leads to deviation from the universality of the PDFs of the different systems.

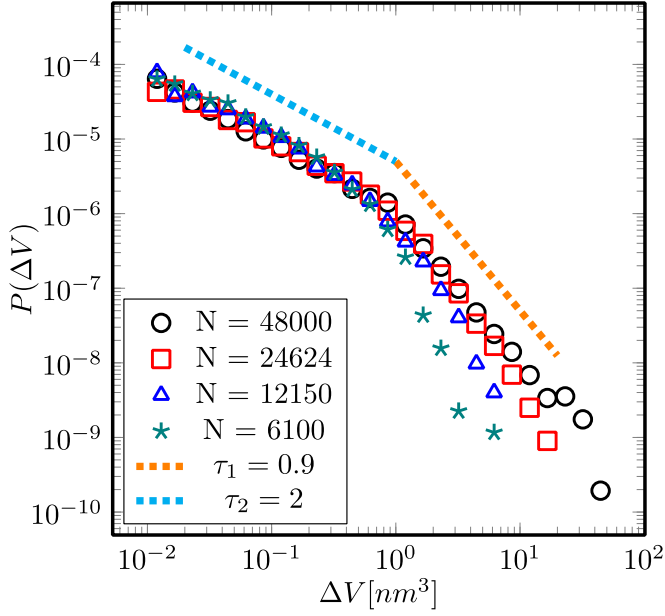


FIG. 8. Probability distribution function for the volume avalanches. The measurements are integrated over the whole loading regime, i.e., until complete failure of the samples. The distribution is not well approximated by a simple power law and instead appears to follow a double power law.

enough number of events to represent the statistics. Accordingly, we keep reducing the strain range until the inclination of the PDF in the log-log plot saturates at $\Delta\varepsilon = 0.005$. We chose the biggest system for this computation since it has the biggest range, over which the lower and upper cutoffs have a small influence. We found that the critical exponent takes a value of $\tau_{\Delta\Pi} \approx 1.4$. From this value, one can compute the exponent $\kappa_{\Delta\Pi} = 1/(\tau'_{\Delta\Pi} - \tau_{\Delta\Pi}) \approx 2.85$. This deviates from the MFT predictions for both the FBM and depinning models, which predict $\tau = 1.5$ and $\kappa = 1.0$ [53] and $\tau = 1.5$ and $\kappa = 2.0$ [61], respectively. Similarly, by repeating the procedure for the stress drops, one obtains the values $\tau_{\Delta\sigma} = 1.27$ and $\kappa_{\Delta\sigma} = 40$. By analyzing the critical exponents pertaining to both the energy and stress drops, it is apparent that a significant deviation from the mean-field exponents $\tau = 1.5$ is present. This is not surprising since it is known that numerous models and simulations do not conform to mean-field calculations. Furthermore, it was shown that damping in sheared glasses affects the critical behavior [65], where overdamped systems have an exponent $\tau = 1.25$ even though the critical behavior is preserved. However, to prove these results, one has to rule out the effect of the initial notch since it favors a localizing effect leading to a concentration of events near the crack tip. Short-range interactions could dominate the system due to an initial crack, leading to failure of the mean-field predictions comparable to the fiber-bundle model with local load-sharing rules if one initially removes some of the fibers. To investigate this effect, we conducted more simulations for the system with 48 000 particles without an initial crack and again computed the critical exponents. The results show that the influence on $\tau_{\Delta\Pi}$ is negligible, which is almost identical to the exponent computed from the notched samples at a value of 1.4. However, a considerable difference appears in the computation of

$\kappa_{\Delta\Pi}$ which has a value of 2.2. As for the stress avalanches, the PDFs are obviously different for the notched specimen. The value of the exponent is $\tau_{\Delta\sigma} = 1.43$, while $\kappa_{\Delta\sigma} = 2.1$. This indicates that the initial notch drives the avalanche exponents of the stress drops away from the MF predictions. This increase in the slope of the avalanche PDF corresponds to the predictions made in the FBM with the local load-sharing rule in the presence of an initial crack [66]. However, this effect is less pronounced for the exponents of the energy drops, affecting rather $\kappa_{\Delta\Pi}$ than $\tau_{\Delta\Pi}$. Moreover, it seems that the difference between the energy and stress avalanche statistics almost vanishes without an initial crack. To explore this aspect further, we computed the Pearson correlation coefficient [67], between the energy drops and stress drops and found consistently high linear correlations $r \approx 0.99$ across all the systems when considering all the avalanche sizes. However, considering only the largest avalanche from each sample, we obtain lower values $r \approx 0.93$ – 0.98 where the smallest system has the lowest linear correlation. Indicating that the effect is stronger for smaller sample sizes due to the larger relative size of the initial crack, which leads to a distortion of the stress avalanche statistics. We conclude that the strength of the disorder in the system was not enough to suppress the perturbing effect of the initial crack on the distribution of the avalanches over the shape and the size of the simulation cell, even though the size was deliberately kept to a minimum while still constituting a critical crack for the failure of the system.

Now we turn our attention to the dependence of the avalanche PDF on the external field, i.e., the strain in our case, by plotting the PDFs for different strain bins. We expect the PDFs to take the following form $P(m, \varepsilon) \sim m^{-\tau-1/k} \{ \gamma[1/k, Am(\varepsilon_c - \varepsilon)] - \gamma(1/k, Am(\varepsilon_c)) \}$, where τ , κ , and ε_c were computed previously and A remains unknown.

To investigate this further, the scaling relation between the average avalanche size and the strain is explored. As a first step, we test the fiber bundle relation $\langle m \rangle \sim (\varepsilon_c - \varepsilon)^\gamma$. However, we find a disagreement of our data with this relation, where one would expect a linear plot on a double logarithmic scale (at least in the asymptotic limit for large-enough events) if the power law were to hold [4]. Instead, we find that the average avalanche size follows an exponential relation, diverging as the systems approach the critical strain range. The average stress avalanche size and the energy avalanche size versus strain are plotted in Fig. 9. It is shown that the average avalanche size diverges between the different sample sizes close to the critical strain. This is qualitatively consistent with Eq. (9), which is derived by analyzing the first moment of the strain-dependent PDF by assuming an exponential cutoff at a critical avalanche size m_c . Therefore, we fitted the constant A of this function for the values of the critical exponents $\tau_{\Delta\Pi}$, $\kappa_{\Delta\Pi}$, and ε_c computed before. For the constant A , we obtained the values 251.5, 124.7, 88.7, and 38.94 for the systems of sizes 48 000, 24 624, 12 150, and 6100, respectively.

To validate the obtained fits and the derived equations, one can plot the PDFs of the energy avalanches conditioned by the strain. This can be seen in Fig. 10, where markers represent PDFs recorded from zero strain to different strain

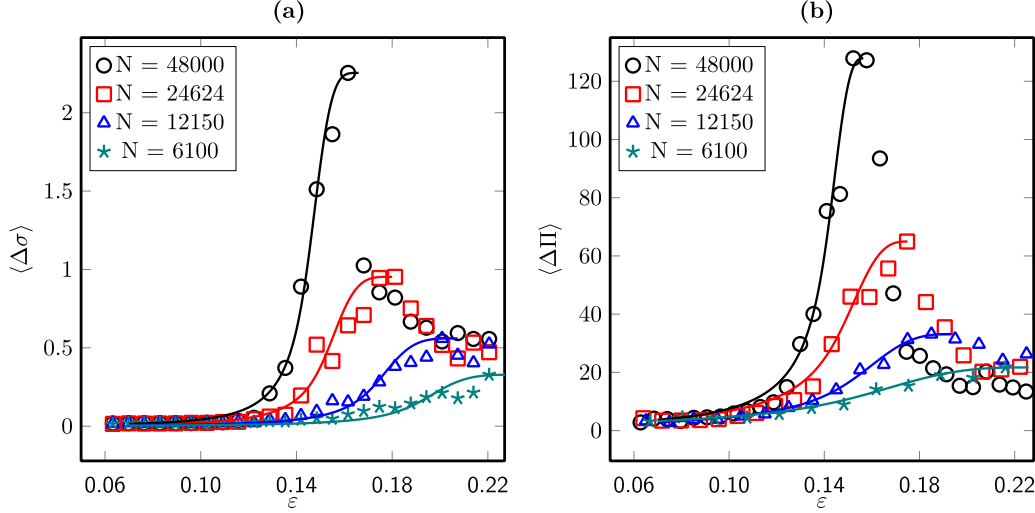


FIG. 9. The average avalanche size as a function of the strain for the stress avalanches in (a) and the energy avalanches in (b). The lines represent the best fit for the exponents κ and A of the function $(\varepsilon_c - \varepsilon)^{\kappa(\tau - a - 1)} \gamma[a - \tau + 1, Am_c(\varepsilon_c - \varepsilon)^\kappa]$ and are obtained for $\kappa_{\Delta \Pi} = 2.85$ for the energy avalanches and $\kappa_{\Delta \sigma} = 4.0$ for the stress avalanches.

threshold values until reaching the critical strain. The lines in Fig. 10 represent the derived function with the computed critical exponents and A . It is evident that this function gives a reasonable fit for the provided data.

The results of this paper show that avalanche statistics of the molecular system can be qualitatively explained by statistical models presented in this paper. At first glance, it might seem improbable that a model based on stick-slip motion, traditionally used to describe earthquake statistics, might help explain fracture statistics. Intriguingly, earthquake dynamics and the deformation mechanism of glasses on the nanoscale share essential statistical similarities [68]. It is conjectured that both systems contain regions susceptible to sudden mechanically induced local structural changes. Under external loading, the system responds elastically until a local stress threshold in these spots is exceeded leading to local inelastic rearrangements. These rearrangements affect other regions in the system through long-range elastic fields [10,37,61]. Despite the complexity of both system types, the

long-range elastic fields could lead to mean-field behavior, rendering many of the microscopic details of the system irrelevant [10,56]. This makes predictions of the statistics of both systems possible, incorporating simplified mean-field calculations that assume an infinite interaction range.

However, extending the molecular systems of this paper to be more transferable to practical demands is a subsequent sensible objective. This way, ambient conditions and glasses with more realistic chemical compositions, such as borosilicates, for example, are of interest.

Notably, we assumed two major simplifications for the molecular models of this paper. The first major simplification is the athermal, overdamped condition. The temperature is known to play an essential role in both the crack propagation and the scaling laws. Indeed, finite temperatures could lead the system to jump over the free energy barrier near the spinodal point, effectively distorting the power laws. However, some fracture experiments at finite temperatures were performed that show that the acoustic emissions, which are thought to

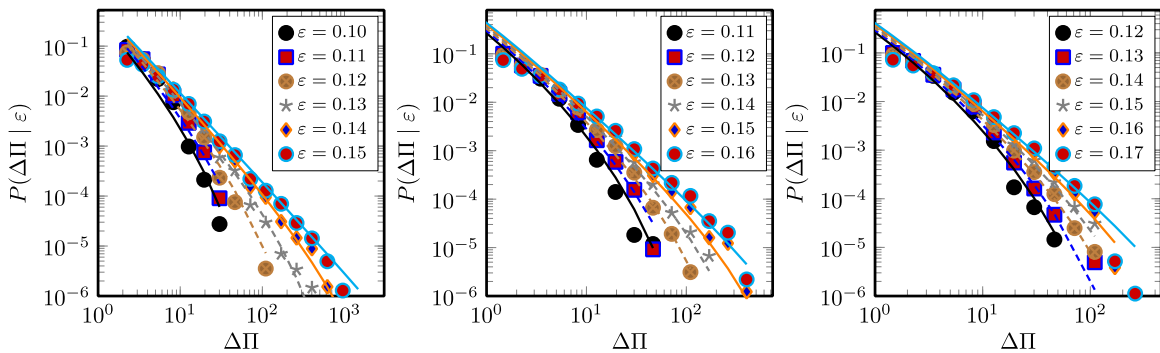


FIG. 10. Energy avalanche PDFs for systems with (a) 48 000, (b) 24 624, and (c) 12 150 particles, integrated up to different strain thresholds, represented by the markers. The solid lines are the scaling functions derived from the assumed exponential cutoff $m^{-\tau-1/k} \{\gamma[1/k, Am(\varepsilon_c - \varepsilon)] - \gamma[1/k, Am(\varepsilon_c)]\}$ with the universal exponents $\tau_{\Delta \Pi} = 1.4$, $\kappa_{\Delta \Pi} = 2.85$, which was computed from the moment analysis in Eq. (9). The value ε_c is system-dependent and is shown in Fig. 3. The parameter A is a system-dependent nonuniversal constant computed through fitting and shown in Fig. 9.

correspond to the energy dissipated in the avalanche events of fracture, obey power laws [69,70], indicating a critical phenomenon.

The second simplification is the pure composition of silica, containing only silicon and oxygen atoms. The introduction of impurities, such as calcium or barium atoms, which induce network depolymerization, may have a significant influence on the fracture statistics. Such chemical modifications alter the average atomic coordination number and affect the ductility of the system. However, studying these factors individually, is an essential step towards understanding the broader and more complex system.

IV. CONCLUSION

We studied the fracture process of silica glass on the nanoscale and revealed several important findings. We showed that the avalanches follow power-law statistics, indicating that our systems exhibit critical behavior. However, due to the short period of the steady state before failure, we ruled out a self-organized critical behavior, which is a phenomenon that is usually observed during the plastic yielding of sheared glasses. However, our systems show some plastic deformation accompanying the fracture process, which manifests in permanent anisotropic changes in the glass Si-O-Si triplets. These changes should be considered when choosing an order parameter to study the yielding transition. Furthermore, the results of the computed critical exponents indicate that the approach to failure in the systems without a notch could be described by depinning models and possibly belong to the same universality class. However, a peculiar behavior is observed for prenotched systems, where a higher value of the avalanche exponential cutoff exponent κ is computed. This increase means that power laws decay faster as the system approaches the critical point since the system fails earlier and large events are less likely to occur. Moreover, the initial notch has a more pronounced effect on the stress avalanches than the energy avalanches. Accordingly, $\tau_{\Delta\Gamma}$ demonstrates a minor deviation from the mean-field exponent, while $\tau_{\Delta\sigma}$ diverges significantly. This finding indicates that a nucleated crack leads not only to the localization of stresses but also perturbs the avalanche statistics. Thus, the avalanches are better studied by analyzing the dissipated energy. Moreover, the derived relations of the strain-conditioned probability density functions and average avalanche sizes show that the scaling relations, derived from the FBM, fit our results qualitatively. However, mean-field depinning models provide similar predictions with a different exponent $\kappa = 2$ [28], providing further evidence that they can capture the avalanche statistics of the current study. However, further analysis of the waiting time exponents and the average temporal shape of the avalanches is necessary to confirm the validity of these models.

We found that the maximum stress near the crack tip decay in the form of a power law with the exponent γ taking values between 0.48 and 0.55 reminiscent of the Irwin formula [63], even though our systems are not ideally brittle and clearly show plasticity with the crack propagation. Furthermore, we computed fracture energies for our systems between 2.84 and 3.04 Joule/m². While these values are much smaller than the experimental values, we cannot exclude that

this effect is caused by the absence of temperature in the simulation.

An important issue that should be addressed in future studies is the discrepancy between the computed fractal dimension and the established values. We postulate that this is caused by the initial notch, which leads to smaller critical avalanches. This phenomenon is expected to have a stronger effect in smaller systems, leading to overestimating the fractal dimension. However, it is also crucial here to conduct additional investigations to confirm the origin of this inconsistency.

Furthermore, we made intriguing observations regarding the scaling laws associated with crack growth avalanches. In these observations, different scaling behavior is observed for the small and large avalanche regimes, as shown in Fig. 8. Intriguingly, this finding connects with a previous study published by Rountree *et al.* [44], in which two different values for the crack roughness for two different scales of silica glass were found. Therefore, further exploring the relationship between crack volume avalanche statistics and crack fractal geometry could provide valuable insights into the underlying mechanisms of crack growth.

We finally conclude that the observed scaling law indicates the occurrence of a phase transition during the fracture process of silica glass. However, the exact nature of this transition remains unclear at this stage, given that the athermal quasistatic framework, together with finite long-range interactions, could bring our systems close to the spinodal point, which is associated with power laws of the avalanches similar to the second-order transition. Therefore, further research is needed to determine the order of this transition and potential crossover regions at even larger scales, considering that our systems exhibit increased brittleness on larger scales.

ACKNOWLEDGMENTS

This research was funded by the Deutsche Forschungsgemeinschaft (DFG, German Research Foundation) Project No. (523939420). Furthermore, the computations were performed with computing resources granted by RWTH Aachen University under Project No. p0020324.

APPENDIX A: MOMENTS ANALYSIS

According to fiber bundle model, the PDF of avalanches bigger than a certain threshold has the following form:

$$P(m, \varepsilon) \sim m^{-\tau} f[Am(\varepsilon_c - \varepsilon)^\kappa], \quad (\text{A1})$$

where $f[Am(\varepsilon_c - \varepsilon)^\kappa]$ is the upper cutoff function. This can be written as

$$\begin{aligned} P(m, \varepsilon) &\sim A^{-1} (\varepsilon_c - \varepsilon)^{\tau\kappa} (Am(\varepsilon_c - \varepsilon)^\kappa)^{-\tau} f(Am(\varepsilon_c - \varepsilon)^\kappa), \\ &\sim (\varepsilon_c - \varepsilon)^{\tau\kappa} g(Am(\varepsilon_c - \varepsilon)^\kappa). \end{aligned} \quad (\text{A2})$$

As a consequence, the first moment of the PDF can be written as

$$\begin{aligned} \langle m^a \rangle &\sim \int_0^{m_c} m^a P(m, \varepsilon) dm, \\ &\sim \int_0^{m_c} (\varepsilon_c - \varepsilon)^{\tau\kappa} m^a g(Am(\varepsilon_c - \varepsilon)^\kappa) dm. \end{aligned} \quad (\text{A3})$$

If we do a variable change, $z = Am(\varepsilon_c - \varepsilon)^\kappa$ so $m = A^{-1}z(\varepsilon_c - \varepsilon)^{-\kappa}$ and $dm = A^{-1}(\varepsilon_c - \varepsilon)^{-\kappa} dz$. It follows

$$\begin{aligned} \langle m^a \rangle &\sim A^{-1} \int_0^{z_c} (\varepsilon_c - \varepsilon)^{\kappa(\tau-a-1)} z^a g(z) dz, \\ &\sim (\varepsilon_c - \varepsilon)^{\kappa(\tau-a-1)} \int_0^{z_c} z^a g(z) dz. \end{aligned} \quad (\text{A4})$$

From the FBM, $f(z)$ is an exponential function e^{-z} , so $g(z)$ would be $z^{-\tau} e^{-z}$:

$$\langle m^a \rangle \sim (\varepsilon_c - \varepsilon)^{\kappa(\tau-a-1)} \int_0^{z_c} z^{a-\tau} e^{-z} dz, \quad (\text{A5})$$

where $z_c = Am_c(\varepsilon_c - \varepsilon)^\kappa$. Then, for all values $(a - \tau + 1 > 0)$ it follows that

$$\int_0^{z_c} z^{a-\tau} e^{-z} dz = \gamma[a - \tau + 1, Am_c(\varepsilon_c - \varepsilon)^\kappa], \quad (\text{A6})$$

where $\gamma[a - \tau + 1, Am_c(\varepsilon_c - \varepsilon)^\kappa]$ is the lower incomplete gamma function. So the first moment of the PDF is written as

$$\langle m^a \rangle \sim (\varepsilon_c - \varepsilon)^{\kappa(\tau-a-1)} \gamma[a - \tau + 1, Am_c(\varepsilon_c - \varepsilon)^\kappa]. \quad (\text{A7})$$

APPENDIX B: STRAIN DEPENDENCE

Starting from Eq. (A1) and integrating over the strain range 0 to ε_c :

$$\begin{aligned} P(m, \varepsilon) &\sim \int_0^{\varepsilon_c} m^{-\tau} f(Am(\varepsilon_c - \varepsilon)^\kappa) d\varepsilon, \\ &\sim m^{-\tau} \int_0^{\varepsilon_c} e^{-Am(\varepsilon_c - \varepsilon)^\kappa} d\varepsilon, \end{aligned}$$

$$\begin{aligned} &\sim m^{-\tau} \int_{Am\varepsilon_c^\kappa}^0 (\kappa^{-1} A^{-1} m^{-1/\kappa} z^{1/\kappa-1} e^{-z} dz), \\ &\sim \kappa^{-1} A^{-1} m^{-\tau} m^{-1/\kappa} \int_{Am\varepsilon_c^\kappa}^0 z^{1/\kappa-1} e^{-z} dz, \\ &\sim m^{-\tau-1/\kappa} \int_{Am\varepsilon_c^\kappa}^0 z^{1/\kappa-1} e^{-z} dz, \\ &\sim m^{-\tau-1/\kappa} \gamma(1/\kappa, Am\varepsilon_c^\kappa). \end{aligned} \quad (\text{B1})$$

Similarly, for arbitrary bin sizes $\varepsilon_2 - \varepsilon_1$:

$$\begin{aligned} P(m, \varepsilon) &\sim m^{-\tau-1/\kappa} \int_{Am(\varepsilon_c - \varepsilon_1)^\kappa}^{Am(\varepsilon_c - \varepsilon_2)^\kappa} z^{1/\kappa-1} e^{-z} dz, \\ &\sim m^{-\tau-1/\kappa} \left(\int_0^{Am(\varepsilon_c - \varepsilon_2)^\kappa} z^{1/\kappa-1} e^{-z} dz \right. \\ &\quad \left. - \int_0^{Am(\varepsilon_c - \varepsilon_1)^\kappa} z^{1/\kappa-1} e^{-z} dz \right), \\ &\sim m^{-\tau-1/\kappa} \{ \gamma[1/\kappa, Am(\varepsilon_c - \varepsilon_2)^\kappa] \\ &\quad - \gamma[1/\kappa, Am(\varepsilon_c - \varepsilon_1)^\kappa] \}. \end{aligned} \quad (\text{B2})$$

Finally, if $\varepsilon_1 = 0$, the PDF is written as

$$\begin{aligned} P(m, \varepsilon) &\sim m^{-\tau-1/\kappa} \{ \gamma(1/\kappa, Am(\varepsilon_c - \varepsilon)^\kappa) \\ &\quad - \gamma[1/\kappa, Am(\varepsilon_c)^\kappa] \}. \end{aligned} \quad (\text{B3})$$

-
- [1] H. J. Herrmann and S. Roux, *Statistical Models for the Fracture of Disordered Media* (North-Holland, Amsterdam 1990).
- [2] A. A. Griffith, *Philos. Trans. R. Soc. London A* **221**, 163 (1921).
- [3] R. L. Blumberg Selinger, Z.-G. Wang, W. M. Gelbart, and A. Ben-Shaul, *Phys. Rev. A* **43**, 4396 (1991).
- [4] S. Zapperi, P. Ray, H. E. Stanley, and A. Vespignani, *Phys. Rev. E* **59**, 5049 (1999).
- [5] F. Bamer, F. Ebrahim, B. Markert, and B. Stamm, *Arch. Comput. Methods Eng.* **30**, 2105 (2023).
- [6] A. Petri, G. Paparo, A. Vespignani, A. Alippi, and M. Costantini, *Phys. Rev. Lett.* **73**, 3423 (1994).
- [7] G. Cannelli, R. Cantelli, and F. Cordero, *Phys. Rev. Lett.* **70**, 3923 (1993).
- [8] M. L. Falk and J. S. Langer, *Phys. Rev. E* **57**, 7192 (1998).
- [9] J. P. Sethna, K. A. Dahmen, and C. R. Myers, *Nature (London)* **410**, 242 (2001).
- [10] D. S. Fisher, K. A. Dahmen, S. Ramanathan, and Y. Ben-Zion, *Phys. Rev. Lett.* **78**, 4885 (1997).
- [11] N. Friedman, S. Ito, B. A. W. Brinkman, M. Shimono, R. E. Lee De Ville, K. A. Dahmen, J. M. Beggs, and T. C. Butler, *Phys. Rev. Lett.* **108**, 208102 (2012).
- [12] P. Bak and K. Sneppen, *Phys. Rev. Lett.* **71**, 4083 (1993).
- [13] D. Richard, M. Ozawa, S. Patinet, E. Stanifer, B. Shang, S. A. Ridout, B. Xu, G. Zhang, P. K. Morse, J.-L. Barrat, L. Berthier, M. L. Falk, P. Guan, A. J. Liu, K. Martens, S. Sastry, D. Vandembroucq, E. Lerner, and M. L. Manning, *Phys. Rev. Mater.* **4**, 113609 (2020).
- [14] S. Patinet, D. Vandembroucq, and M. L. Falk, *Phys. Rev. Lett.* **117**, 045501 (2016).
- [15] G. Kapteijns, D. Richard, and E. Lerner, *Phys. Rev. E* **101**, 032130 (2020).
- [16] D. Richard, G. Kapteijns, J. A. Giannini, M. L. Manning, and E. Lerner, *Phys. Rev. Lett.* **126**, 015501 (2021).
- [17] L. Tian, Y. Fan, L. Li, and N. Mousseau, *Scr. Mater.* **186**, 185 (2020).
- [18] C. Tang and P. Bak, *J. Stat. Phys.* **51**, 797 (1988).
- [19] H. E. Stanley, *Introduction to Phase Transitions and Critical Phenomena* (Oxford University Press, Oxford, 1987).
- [20] P. Bak, C. Tang, and K. Wiesenfeld, *Phys. Rev. Lett.* **59**, 381 (1987).
- [21] C. Tang and P. Bak, *Phys. Rev. Lett.* **60**, 2347 (1988).
- [22] P. Bak, *How Nature Works: The Science of Self Organized Criticality* (Copernicus Press, New York, 1996).
- [23] B. A. Sun, H. B. Yu, W. Jiao, H. Y. Bai, D. Q. Zhao, and W. H. Wang, *Phys. Rev. Lett.* **105**, 035501 (2010).
- [24] J. Lin, E. Lerner, A. Rosso, and M. Wyart, *Proc. Natl. Acad. Sci. USA* **111**, 14382 (2014).
- [25] Z. Budrikis, D. Fernández Castellanos, S. Sandfeld, M. Zaiser, and S. Zapperi, *Nat. Commun.* **8**, 15928 (2017).

- [26] H. G. E. Hentschel, S. Karmakar, E. Lerner, and I. Procaccia, *Phys. Rev. Lett.* **104**, 025501 (2010).
- [27] N. Oyama, H. Mizuno, and A. Ikeda, *Phys. Rev. E* **104**, 015002 (2021).
- [28] I. Regev, J. Weber, C. Reichhardt, K. A. Dahmen, and T. Lookman, *Nat. Commun.* **6**, 8805 (2015).
- [29] C. Liu, E. E. Ferrero, F. Puosi, J. L. Barrat, and K. Martens, *Phys. Rev. Lett.* **116**, 065501 (2016).
- [30] H. Xu, J. C. Andresen, and I. Regev, *Phys. Rev. E* **103**, 052604 (2021).
- [31] G. P. Shrivastav, P. Chaudhuri, and J. Horbach, *Phys. Rev. E* **94**, 042605 (2016).
- [32] T. Niiyama, M. Wakeda, T. Shimokawa, and S. Ogata, *Phys. Rev. E* **100**, 043002 (2019).
- [33] M. J. Demkowicz and A. S. Argon, *Phys. Rev. B* **72**, 245206 (2005).
- [34] H. Bhaumik, G. Foffi, and S. Sastry, *Phys. Rev. Lett.* **128**, 098001 (2022).
- [35] S. Bonfanti, E. E. Ferrero, A. L. Sella, R. Guerra, and S. Zapperi, *Nano Lett.* **18**, 4100 (2018).
- [36] Z. Budrikis and S. Zapperi, *Phys. Rev. E* **88**, 062403 (2013).
- [37] J. Antonaglia, W. J. Wright, X. Gu, R. R. Byer, T. C. Hufnagel, M. LeBlanc, J. T. Uhl, and K. A. Dahmen, *Phys. Rev. Lett.* **112**, 155501 (2014).
- [38] J. Antonaglia, X. Xie, G. Schwarz, M. Wraith, J. Qiao, Y. Zhang, P. K. Liaw, J. T. Uhl, and K. A. Dahmen, *Sci. Rep.* **4**, 4382 (2014).
- [39] F. Bamer, F. Ebrahim, and B. Markert, *J. Non-Cryst. Solids* **503-504**, 176 (2019).
- [40] F. Bamer, S. S. Alshabab, A. Paul, F. Ebrahim, B. Markert, and B. Stamm, *Scr. Mater.* **205**, 114179 (2021).
- [41] F. Ebrahim, F. Bamer, and B. Markert, *Phys. Rev. E* **102**, 033006 (2020).
- [42] B. R. Lawn, B. J. Hockey, and S. M. Wiederhorn, *J. Mater. Sci.* **15**, 1207 (1980).
- [43] F. Célarié, S. Prades, D. Bonamy, L. Ferrero, E. Bouchaud, C. Guillot, and C. Marlière, *Phys. Rev. Lett.* **90**, 075504 (2003).
- [44] C. L. Rountree, S. Prades, D. Bonamy, E. Bouchaud, R. Kalia, and C. Guillot, *J. Alloys Compd.* **434-435**, 60 (2007).
- [45] E. Barthel, V. Keryvin, G. Rosales-Sosa, and G. Kermouche, *Acta Mater.* **194**, 473 (2020).
- [46] M. Matsui, *Mineral. Mag.* **58A**, 571 (1994).
- [47] M. Bouhadja, N. Jakse, and A. Pasturel, *J. Chem. Phys.* **138**, 224510 (2013).
- [48] C. E. Maloney and A. Lemaitre, *Phys. Rev. E* **74**, 016118 (2006).
- [49] V. P. Voloshin, A. V. Anikeenko, N. N. Medvedev, and A. Geiger, in *Proceedings of the 2011 Eighth International Symposium on Voronoi Diagrams in Science and Engineering* (IEEE, New York, 2011), pp. 170–176.
- [50] S. Sastry, D. S. Corti, P. G. Debenedetti, and F. H. Stillinger, *Phys. Rev. E* **56**, 5524 (1997).
- [51] N. P. Bailey, J. Schiøtz, A. Lemaitre, and K. W. Jacobsen, *Phys. Rev. Lett.* **98**, 095501 (2007).
- [52] A. Chessa, H. E. Stanley, A. Vespignani, and S. Zapperi, *Phys. Rev. E* **59**, R12 (1999).
- [53] P. C. Hemmer and A. Hansen, *J. Appl. Mech.* **59**, 909 (1992).
- [54] T. Focks, F. Bamer, B. Markert, Z. Wu, and B. Stamm, *Phys. Rev. B* **106**, 014105 (2022).
- [55] C. Unger and W. Klein, *Phys. Rev. B* **29**, 2698 (1984).
- [56] M. J. Alava, P. K. V. V. Nukala, and S. Zapperi, *Adv. Phys.* **55**, 349 (2006).
- [57] S. Zapperi, P. Ray, H. E. Stanley, and A. Vespignani, *Phys. Rev. Lett.* **78**, 1408 (1997).
- [58] R. Dickman, M. A. Muñoz, A. Vespignani, and S. Zapperi, *Braz. J. Phys.* **30**, 27 (2000).
- [59] F. Bamer, F. Ebrahim, and B. Markert, *Materialia* **9**, 100556 (2020).
- [60] J. Lin, A. Saade, E. Lerner, A. Rosso, and M. Wyart, *Europhys. Lett.* **105**, 26003 (2014).
- [61] K. A. Dahmen, Y. Ben-Zion, and J. T. Uhl, *Phys. Rev. Lett.* **102**, 175501 (2009).
- [62] C. L. Rountree, D. Vandembroucq, M. Talamali, E. Bouchaud, and S. Roux, *Phys. Rev. Lett.* **102**, 195501 (2009).
- [63] G. R. Irwin, *J. Appl. Mech.* **24**, 361 (1957).
- [64] Y. Yu, B. Wang, Y. J. Lee, and M. Bauchy, *MRS Online Proc. Library* **1757**, 47 (2014), and references therein.
- [65] K. M. Salerno, C. E. Maloney, and M. O. Robbins, *Phys. Rev. Lett.* **109**, 105703 (2012).
- [66] S. Roy, T. Hatano, and P. Ray, *Phys. Rev. E* **105**, 055003 (2022).
- [67] D. Freedman, R. Pisani, and R. Purves, *Statistics (4th ed.)* (WW Norton, New York 2007).
- [68] J. Uhl, S. Pathak, and D. Schorlemmer *et al.*, *Sci. Rep.* **5**, 16493 (2015).
- [69] I. P. Shcherbakov and A. E. Chmel', *Glass Phys. Chem.* **39**, 527 (2013).
- [70] A. Garcimartín, A. Guarino, L. Bellon, and S. Ciliberto, *Phys. Rev. Lett.* **79**, 3202 (1997).